

The steady propagation of a semi-infinite bubble into a tube of elliptical or rectangular cross-section

By ANDREW L. HAZEL AND MATTHIAS HEIL

Department of Mathematics, University of Manchester, Oxford Road,
Manchester M13 9PL, UK

(Received 15 June 2001 and in revised form 26 April 2002)

This paper investigates the propagation of an air finger into a fluid-filled, axially uniform tube of elliptical or rectangular cross-section with transverse length scale a and aspect ratio α . Gravity is assumed to act parallel to the tube's axis. The problem is studied numerically by a finite-element-based direct solution of the free-surface Stokes equations.

In rectangular tubes, our results for the pressure drop across the bubble tip, Δp , are in good agreement with the asymptotic predictions of Wong *et al.* (1995*b*) at low values of the capillary number, Ca (ratio of viscous to surface-tension forces). At larger Ca , Wong *et al.*'s (1995*b*) predictions are found to underestimate Δp . In both elliptical and rectangular tubes, the ratio $\Delta p(\alpha)/\Delta p(\alpha = 1)$ is approximately independent of Ca and thus equal to the ratio of the static meniscus curvatures.

In non-axisymmetric tubes, the air–liquid interface develops a noticeable asymmetry near the bubble tip at all values of the capillary number. The tip asymmetry decays with increasing distance from the bubble tip, but the decay rate becomes very small as Ca increases. For example, in a rectangular tube with $\alpha = 1.5$, when $Ca = 10$, the maximum and minimum finger radii still differ by more than 10% at a distance $100a$ behind the finger tip. At large Ca the air finger ultimately becomes axisymmetric with radius r_∞ . In this regime, we find that r_∞ in elliptical and rectangular tubes is related to r_∞ in circular and square tubes, respectively, by a simple, empirical scaling law. The scaling has the physical interpretation that for rectangular and elliptical tubes of a given cross-sectional area, the propagation speed of an air finger, which is driven by the injection of air at a constant volumetric rate, is independent of the tube's aspect ratio.

For smaller Ca ($Ca < \widehat{Ca}$), the air finger is always non-axisymmetric and the persisting draining flows in the thin film regions far behind the bubble tip ultimately lead to dry regions on the tube wall. \widehat{Ca} increases with increasing α and for $\alpha > \hat{\alpha}$ dry spots will develop on the tube walls at all values of Ca .

1. Introduction

We consider the steady motion of long bubbles in rigid tubes of constant cross-section. The aim of the study is to determine the shape of the air–liquid interface and the pressure drop across the bubble tip as a function of capillary number, Ca (the ratio of viscous to surface-tension forces) in rectangular and elliptical tubes. Our numerical study complements the previous small- Ca asymptotic work of Wong, Radke & Morris

(1995*a,b*) and extends their results to $O(1)$ capillary numbers. We restrict attention to flows in which inertial effects may be neglected, although the formulation and the numerical method could readily be extended to finite-Reynolds-number flows.

Applications include biomechanics, coating processes, enhanced oil recovery and flows in porous media on the pore scale. An important biological application is the airway reopening problem (Gaver, Samsel & Solway 1990; Gaver *et al.* 1996), the main motivation for our study. Many lung diseases can cause the smaller airways to collapse non-axisymmetrically and become occluded by the fluid that lines them. A long finger of air is believed to reopen the collapsed airway by redistributing the fluid of the blockage as it propagates. The precise details of this mechanism are still unclear, partly because all existing studies of this problem are based on two-dimensional models.

Bubble propagation in circular tubes has been comprehensively investigated using theoretical (e.g. Bretherton 1961; Park & Homsy 1984; Ratulowski & Chang 1989), experimental (e.g. Cox 1962; White & Beardmore 1962; Goldsmith & Mason 1963; Chen 1986; Schwartz, Princen & Kiss 1986) and numerical techniques (e.g. Reinelt & Saffman 1985; Shen & Udell 1985; Westborg & Hassager 1989; Giavedoni & Saita 1997). In contrast, bubble propagation in non-axisymmetric tubes has received considerably less attention. Furthermore, all previous studies of bubble propagation in non-axisymmetric tubes used either experimental methods or asymptotic approximations valid only at small capillary numbers (e.g. Singhal & Sommerton 1970; Kolb & Cerro 1991, 1993; Ratulowski & Chang 1989; Wong *et al.* 1995*a,b*).

In every tube geometry, the radius of the propagating air finger increases as the capillary number decreases. In the (singular) limit $Ca \rightarrow 0$, corresponding to infinite surface tension, or a propagation speed of zero, the shape of the air-liquid interface approaches that of the static equilibrium configuration. This fact was exploited by Wong *et al.* (1995*a,b*), who were able to develop a small- Ca asymptotic description of the interface evolution and pressure drop across the bubble tip by perturbing about previously computed static equilibrium shapes in polygonal tubes (Wong, Morris & Radke 1992).

Wong *et al.*'s (1995*a,b*) solution is directly analogous to Bretherton's (1961) work in circular tubes. Numerical simulations indicate, however, that Bretherton's (1961) asymptotic solution is accurate only at extremely small Ca ($Ca < 10^{-3}$) (e.g. Reinelt & Saffman 1985; Giavedoni & Saita 1997). We believe the present study to be the first to consider steady bubble propagation in rigid tubes of non-axisymmetric cross-section at $O(1)$ Ca and we use our results to investigate the accuracy of Wong *et al.*'s (1995*a,b*) asymptotic solution. Our study should also be regarded as a first step towards an improved model of the fluid flows in the three-dimensional airway reopening problem.

2. The model

The model problem, sketched in figure 1, is that of an air finger moving at a constant speed U , under an internal pressure p_b , into a tube of transverse length scale a . The tube is filled with a Newtonian fluid of viscosity μ , density ρ and the (constant) surface tension at the air-liquid interface is given by γ . (The presence of surfactants may lead to a non-uniform surface tension on the interface, but this effect is neglected in the present work.) The tube is assumed to be open far ahead of the finger tip and fluid is driven out of the tube by the motion of the finger, leaving a film of fluid of thickness h on the tube walls. Gravitational effects are restricted to

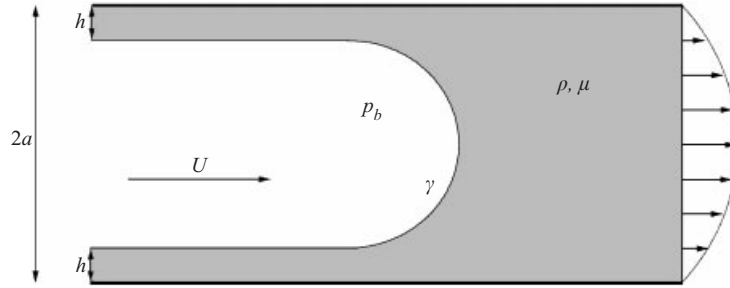


FIGURE 1. Sketch of the problem: an air finger propagates into a tube of constant cross-section and deposits a film of fluid behind the advancing finger tip. In non-circular tubes, the film thickness, h , is non-uniform in the azimuthal direction.

cases in which gravity acts in a direction parallel to the tube axis. This restriction does not break the transverse symmetry of the problem and allows the restriction of the computational domain to one quarter of the tube's cross-section for rectangular and elliptical geometries.

We consider flows in a regime in which inertial forces are negligible. The problem is thus governed by two dimensionless parameters: the capillary number (Ca) and the Bond number (Bo), being the ratios of viscous to surface-tension forces and gravitational to surface-tension forces, respectively:

$$Ca \equiv \frac{\mu U}{\gamma}, \quad Bo \equiv \frac{\rho g a^2}{\gamma}, \quad (2.1)$$

where g is the acceleration due to gravity.

The problem is formulated in dimensionless Cartesian coordinates $\mathbf{x} = (x_1, x_2, x_3) = \mathbf{x}^*/a$ and the finger propagates in the negative x_3 -direction. Hereinafter, an asterisk is used to indicate dimensional quantities, as opposed to their dimensionless equivalents. The fluid velocity is scaled with the bubble velocity, $\mathbf{u} = \mathbf{u}^*/U$, and the internal fluid pressure is scaled on the viscous scale, $p = p^*/(\mu U/a)$.

In a frame moving with the (constant) velocity of the bubble, U , the flow is governed by the dimensionless, steady Stokes equations:

$$-\frac{\partial p}{\partial x_i} + \frac{Bo}{Ca} k_i + \frac{\partial}{\partial x_j} \left(\frac{\partial u_i}{\partial x_j} + \frac{\partial u_j}{\partial x_i} \right) = 0, \quad (2.2a)$$

and the continuity equation

$$\frac{\partial u_i}{\partial x_i} = 0, \quad (2.2b)$$

where $i, j = 1, 2, 3$ and summation convention is used. The unit vector $\mathbf{k} = \mathbf{e}_3$ indicates the direction of gravity so that a positive Bond number corresponds to the case in which the air finger moves against the direction of gravity (upwards).

The free-surface boundary conditions are those of non-penetration

$$u_i n_i = 0 \quad \text{on the free surface}, \quad (2.3a)$$

and the dynamic boundary condition

$$-p n_i + \left(\frac{\partial u_i}{\partial x_j} + \frac{\partial u_j}{\partial x_i} \right) n_j + \frac{1}{Ca} \kappa n_i = -p_b n_i \quad \text{on the free surface}. \quad (2.3b)$$

\mathbf{n} is the unit normal to the free surface (directed out of the fluid); $\kappa = \kappa^* a$ is the

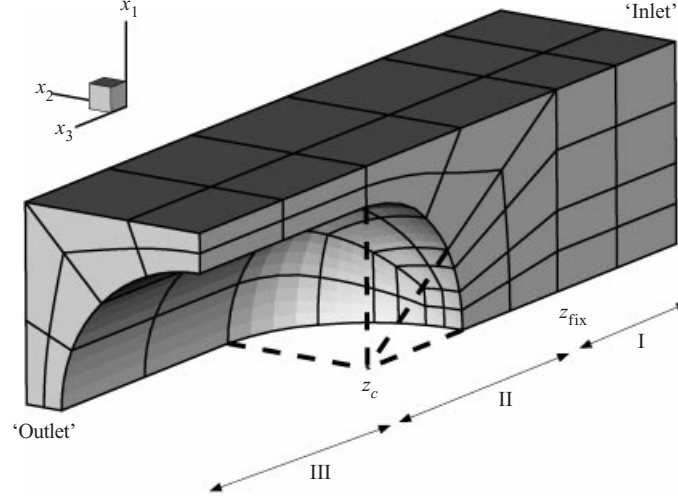


FIGURE 2. Illustration of the coordinate axes and a (coarse) fluid finite-element mesh for an air finger propagating into a rectangular tube.

dimensionless (first) curvature of the surface, the sum of the principal curvatures; and p_b is the dimensionless internal bubble pressure. In the moving frame of reference, the no-slip boundary condition is

$$\mathbf{u} = (0, 0, 1) \quad \text{on the tube walls.} \quad (2.3c)$$

Finally, we locate the bubble tip at the origin by enforcing

$$x_3 = 0 \quad \text{at the bubble tip.} \quad (2.3d)$$

In order to solve these equations numerically, we decompose the fluid domain, shown in figure 2, into a number of finite elements. We exploit symmetry at the planes $x_1 = 0$ and $x_2 = 0$ by restricting the computational domain to positive values of the transverse coordinates: $x_1 \geq 0, x_2 \geq 0$. In region I, $x_3 < z_{\text{fix}}$, the elements remain fixed during the computation. In regions II and III, $x_3 > z_{\text{fix}}$, the position of the free surface affects the fluid domain and the nodal positions are adjusted by the method of spines (Kistler & Scriven 1983). The free surface is parameterized by the distance $h(\zeta_1, \zeta_2)$ from a fixed surface, $\Gamma = \Gamma_1 \cup \Gamma_2$, where Γ_1 is the tube wall in regions II and III and Γ_2 is the dividing plane between regions I and II, $x_3 = z_{\text{fix}}$. We parameterize Γ by two surface coordinates, ζ_1 and ζ_2 , and denote the position vector of any point on Γ by $\mathbf{\Gamma}(\zeta_1, \zeta_2)$. On Γ_1 , ζ_1 and ζ_2 are the polar coordinates, x_3 and $\theta \equiv \tan^{-1}(x_2/x_1)$, whereas on Γ_2 , ζ_1 and ζ_2 are the Cartesian coordinates in the transverse plane, x_1 and x_2 .

The distance h is measured in the direction of the spines, $\mathbf{S}(\zeta_1, \zeta_2)$. Each spine is of unit length and is anchored at a fixed point on Γ . The position of the free surface, \mathbf{R}_{fs} , is then given by

$$\mathbf{R}_{\text{fs}}(\zeta_1, \zeta_2) = \mathbf{\Gamma}(\zeta_1, \zeta_2) + h(\zeta_1, \zeta_2)\mathbf{S}(\zeta_1, \zeta_2). \quad (2.4)$$

It is convenient to decompose Γ into a region close to the bubble tip ($x_3 < z_c$, region II in figure 2) and a downstream region ($x_3 > z_c$, region III in figure 2). In region II, the spines are all directed to a single point $(0, 0, z_c)$, whereas in region III if the base of the spine is at (x_1, x_2, x_3) , the spine is directed towards $(0, 0, x_3)$. These definitions provide a continuous transition between the two regions and the dashed

lines in figure 2 indicate spine directions in region II, showing the intersection at the point $(0, 0, z_c)$. The nodal points of each element in regions II and III are chosen to lie at fixed fractions along the spines. As the free surface deforms, the distance from Γ to the free surface changes and the nodal points adjust to remain at the same fixed fractions along the spine.

We discretize the fluid variables using isoparametric, Taylor–Hood elements (Taylor & Hood 1973), and the spine heights by isoparametric, two-dimensional quadratic elements. The dynamic boundary condition (2.3b) is incorporated into the weak form of the momentum equation by partial integration (Ruschak 1980) to give

$$\begin{aligned} & \iiint \frac{Bo}{Ca} k_i \psi^{(F)} dV + \iiint \left[p \frac{\partial \psi^{(F)}}{\partial x_i} - \left(\frac{\partial u_i}{\partial x_j} + \frac{\partial u_j}{\partial x_i} \right) \frac{\partial \psi^{(F)}}{\partial x_j} \right] dV \\ & + \iint \left[-pn_i + \left(\frac{\partial u_i}{\partial x_j} + \frac{\partial u_j}{\partial x_i} \right) n_j \right] \psi^{(F)} dS_{S_{fs}} \\ & + \frac{1}{Ca} \iint \frac{1}{g} [\mathbf{g}_1]_i \left(g_{22} \frac{\partial \psi^{(F)}}{\partial \zeta_1} - g_{12} \frac{\partial \psi^{(F)}}{\partial \zeta_2} \right) + \frac{1}{g} [\mathbf{g}_2]_i \left(g_{11} \frac{\partial \psi^{(F)}}{\partial \zeta_2} - g_{12} \frac{\partial \psi^{(F)}}{\partial \zeta_1} \right) dS_{fs} \\ & - \iint p_b \psi^{(F)} n_i dS_{fs} - \frac{1}{Ca} \oint \psi^{(F)} m_i ds = 0, \end{aligned} \quad (2.5a)$$

where $\psi^{(F)}$ are the piecewise, tri-quadratic velocity basis functions. The volume integrals are evaluated over the entire computational domain, V ; the surface integrals over the free surface, S_{fs} , or the boundary of the computational domain, excluding the free surface, $S_{\setminus S_{fs}}$; and the line integral over the line bounding the free surface, B .

The covariant base vectors of the free surface, the metric tensor and its determinant are defined by

$$\mathbf{g}_1 = \frac{\partial \mathbf{R}_{fs}}{\partial \zeta_1}, \quad \mathbf{g}_2 = \frac{\partial \mathbf{R}_{fs}}{\partial \zeta_2}, \quad g_{\beta\delta} = \mathbf{g}_\beta \cdot \mathbf{g}_\delta, \quad g = g_{11}g_{22} - g_{12}g_{21},$$

where the indices β and δ take the values 1 or 2. The notation $[\mathbf{g}_\beta]_i$ indicates the i th component of the base vector \mathbf{g}_β . The unit vector \mathbf{m} is tangent to the free surface and normal to the curve B , directed out of the computational domain, see figure 3.

The system is completed by the weak forms of the continuity equation (2.2b) and non-penetration condition on the free surface (2.3a):

$$\iiint \frac{\partial u_i}{\partial x_i} \psi^{(P)} dV = 0 \quad \text{and} \quad \iint u_i n_i \psi^{(H)} dS_{fs} = 0, \quad (2.5b, c)$$

where $\psi^{(P)}$ are the piecewise, tri-linear pressure basis functions and $\psi^{(H)}$ are the piecewise, bi-quadratic basis functions for the spine heights.

2.1. ‘End’ boundary conditions

Far from the bubble tip, the motion becomes independent of the axial coordinate and the axial component of (2.2a) reduces to a Poisson equation:

$$\frac{Bo}{Ca} + \frac{\partial}{\partial x_\beta} \left(\frac{\partial u_3}{\partial x_\beta} \right) = 0, \quad (2.6a)$$

where $\beta = 1, 2$ – the transverse directions. The no-slip boundary condition (2.3c) still applies and becomes

$$u_3 = 1 \quad \text{on the tube walls.} \quad (2.6b)$$

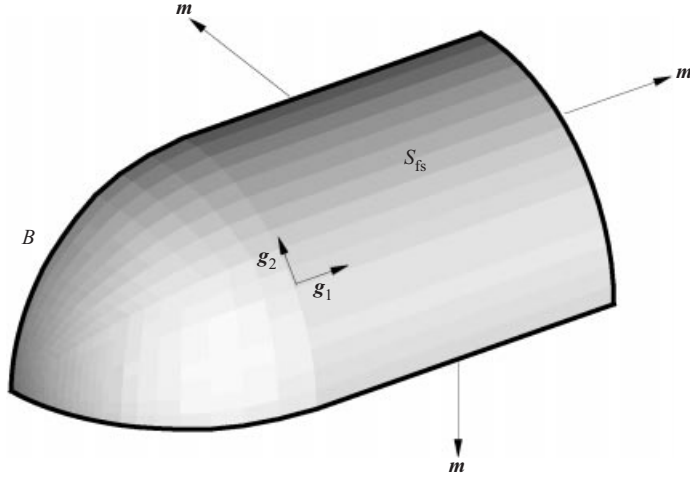


FIGURE 3. The air–liquid interface, S_{fs} , is bounded by the closed curve B and is locally described by the covariant base vectors $\mathbf{g}_1(\zeta_1, \zeta_2)$ and $\mathbf{g}_2(\zeta_1, \zeta_2)$. The vector \mathbf{m} is tangent to S_{fs} , normal to B and directed out of the free surface.

As $x_3 \rightarrow \infty$, the dynamic boundary condition (2.3b), becomes a zero-tangential-stress boundary condition

$$\frac{\partial u_3}{\partial n} = 0 \quad \text{on the air–liquid interface,} \quad (2.6c)$$

where n is the normal to the interface in the transverse plane.

In two-dimensional, or axisymmetric, formulations of similar problems, previous investigators (Reinelt & Saffman 1985; Halpern & Gaver 1994; Heil 2001) have solved the Poisson equation (2.6a) analytically at both the ‘inlet’ ($x_3 \rightarrow -\infty$) and ‘outlet’ ($x_3 \rightarrow \infty$) surfaces. The resulting axial velocity fields are then applied as Dirichlet boundary conditions. In these cases, the ‘inlet’ velocity field is a function of the film thickness behind the air finger and the explicit coupling between the ‘inlet’ and ‘outlet’ ensures that the flux into the domain is equal to the flux out. This approach may be extended to the three-dimensional problem, but, in a general tube cross-section, the two Poisson equations must be solved numerically.

We present an alternative formulation of the boundary conditions that requires the solution of only one Poisson equation and eliminates the direct coupling between the inlet and outlet faces. At the outlet, we solve the Poisson equation (2.6a) to determine the axial velocity profile which we impose as a Dirichlet boundary condition for the axial velocity. In the transverse directions, tractions consistent with the solution of the Poisson equation are imposed, to allow the development of transverse draining flows. (In the zero-Bond-number case, the transverse tractions are identically zero.) At the inlet, the transverse velocity components are set to zero, enforcing parallel flow, but the axial boundary condition is left traction free – the natural boundary condition. Thus, mass is conserved via the continuity equation with no need for direct coupling across the entire domain. The elimination of the explicit upstream–downstream coupling not only avoids the solution of a second Poisson equation but was also found to be beneficial in the frontal solution technique, see §2.2, as it reduces the size of the frontal matrix. A slight subtlety arises from the fact that a traction-free inlet face is equivalent to setting the pressure to zero at the inlet, which is inconsistent with setting the bubble pressure to zero. Thus, p_b must be treated as an

unknown in the problem and an additional equation is required to determine its value. The equation is generated by treating (2.3d) as a residual rather than an essential boundary condition. A similar method was used by Heil (2000) in the simulation of the propagation of an air finger into a flexible-walled channel. This approach has the further advantage of ensuring that $\mathbf{u} \cdot \mathbf{n} = 0$ is enforced, in a weak sense, along the entire air–liquid interface.

2.2. Numerical implementation

The discrete form of the nonlinear system of equations (2.5a–c) is solved by Newton–Raphson iteration. A frontal scheme (Duff & Scott 1996) was used to assemble the Jacobian matrices and solve the resulting linear systems. The frontal solver minimizes memory requirements and was found to be much more efficient than assembling the entire Jacobian matrix before solving. The entries of the Jacobian matrix were assembled analytically, apart from the off-diagonal terms associated with spine variables which were generated by finite differencing. For a typical initial guess, the residuals are of $O(1)$ and the iteration was deemed to have converged when the absolute value of the largest residual was less than 10^{-8} .

A problem involving approximately 20 000 degrees of freedom, our standard resolution, requires about two minutes of CPU time per Newton iteration on a 1.2 GHz Linux PC. This formulation was found to be very robust and starting from an initial interface shape, consisting of a spherical cap matched to a uniform circular cylinder, a converged solution is typically obtained within 5 iterations. Once a converged solution is obtained, a continuation technique is used to incrementally step through different values of the capillary and Bond numbers.

A large number of tests were conducted to validate the newly developed code. These included (i) the computation of flows in uniform tubes in the absence of the air–liquid interface; (ii) capillary statics problems in which the in- and outflow velocities were set to zero; and (iii) comparisons of axisymmetric results with those of other studies, see § 3.1. The spatial convergence of all results was ensured by repeating selected cases with a finer spatial resolution (see figure 7(a) and Appendix A).

Finally, the effect of the downstream length of the computational domain upon the results was investigated, with particular attention paid to the development of draining flows in non-axisymmetric geometries. It was found that the boundary conditions described in § 2.1 are rather forgiving and that the solution at a given position was not affected by an increase in the length of the computational domain; see figure 7(b). Thus, studies of the flow close to the finger tip could be conducted in relatively short domains.

3. Results and discussion

3.1. Axisymmetric tube (validation)

The problem of bubble propagation in an axisymmetric (circular) tube has been widely studied and is here used to validate the numerical method described in § 2. The governing equations (2.2a,b) are formulated in Cartesian coordinates and the computation of axisymmetric solutions is, therefore, a non-trivial validation of the general three-dimensional code. Bretherton (1961) used lubrication theory and simple matching to derive the expressions

$$h_{\infty} = 1.3375 Ca^{2/3} \quad \text{and} \quad \Delta p_{ca} = 2 + 7.4467 Ca^{2/3} \quad \text{as} \quad Ca \rightarrow 0, \quad (3.1a, b)$$

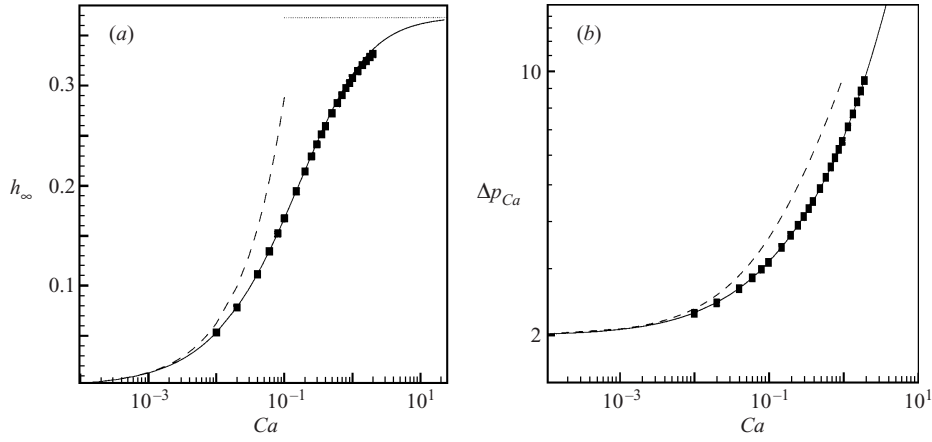


FIGURE 4. Results for a circular tube: (a) film thickness far from the finger tip and (b) pressure drop (on the capillary scale) across the finger tip plotted against capillary number (solid line). Bretherton's theoretical result for low Ca is shown as a dashed line and the numerical results of Reinelt & Saffman (1985) are shown as boxes. Cox's (1962) experimental asymptote for film thickness at high Ca is the horizontal grey line in (a).

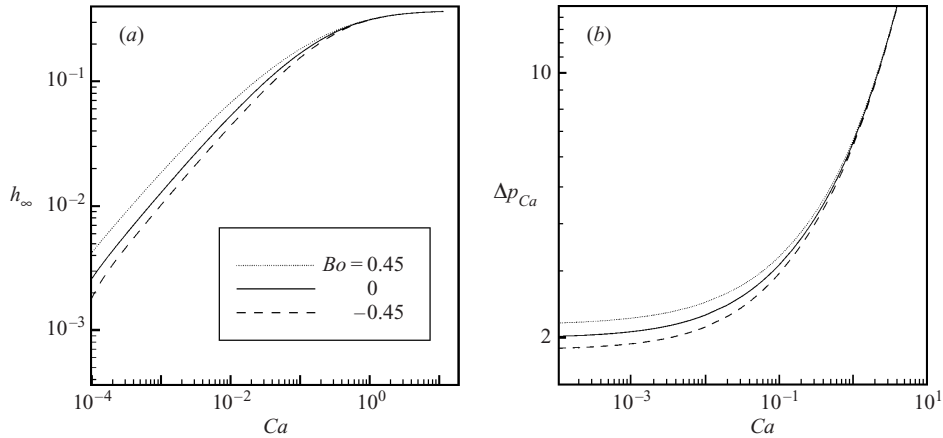


FIGURE 5. Effects of gravity in a circular tube: (a) film thickness far from the finger tip and (b) pressure drop (on the capillary scale) across the finger tip plotted against capillary number. The results for Bond numbers of 0.45, -0.45 and 0 are shown.

where h_∞ is the film height far behind the finger tip and $\Delta p_{Ca} = \Delta p^*/(\gamma/a)$ is the pressure drop across the tip on the capillary scale. Figure 4 shows our numerical results, equations (3.1a,b) and the results from the axisymmetric computations of Reinelt & Saffman (1985). The high-capillary-number asymptote for h_∞ , found experimentally by Cox (1962), is also shown in figure 4(a). The agreement with previous numerical results is good over the entire range of Ca (relative error less than 1%) and at $Ca = 10$, $h_\infty = 0.361$, in agreement with the computations of Giavedoni & Saita (1997).

Figure 5 shows the effects of gravity upon the film thickness and pressure drop across the finger tip. In the majority of physiological and industrial applications, these effects are expected to be minor owing to the relatively small radii of the vessels concerned. The values of $Bo = \pm 0.45$ are those used in Kolb & Cerro's (1991)

experimental study. For positive Bond numbers, corresponding to a bubble travelling upwards, the main effect of gravity is to cause an additional flow into the film surrounding the bubble and hence a thickening of the film and an increase in the pressure drop across the finger tip. Bretherton (1961) obtained the correction term $1 + \frac{2}{3}Bo$ for the film thickness, in the low-capillary-number limit, although he gives no explanation of its derivation. For a bubble travelling downwards ($Bo < 0$), gravity causes less fluid to enter the film; hence its thickness is reduced and the pressure drop decreases.

The Bond number only enters the governing equations (2.2a,b) in the dimensionless grouping Bo/Ca and so at high values of the capillary number, gravitational effects become unimportant compared to the balance of viscous and surface-tension forces. Thus, the data collapse onto a single line as the capillary number increases. At the lowest value of Ca shown in figure 5 ($Ca = 10^{-4}$) there is a noticeable difference in film thicknesses among the three cases. The film thicknesses do not agree with the correction term of Bretherton, however, presumably because the Bond number is too large. Thulasidas, Abraham & Cerro (1995) conducted experiments in circular tubes with a Bond number of 0.43 and also concluded that this value was too large to expect agreement with Bretherton's theory.

In order to validate the non-zero Bond number computations, we reproduced the results of Reinelt (1987) for the purely buoyant rise of a long bubble in a sealed circular tube. The problem in a sealed tube is a special case of that in an open tube in which the upward flux of fluid due to the bubble motion exactly balances the downward flux due to gravity. In a stationary frame of reference, therefore, the net axial flow rate, Q , will be zero and the corresponding flow rate in the computational domain is $Q_c = \pi/4$. At a given Ca , the (unique) value of Bo such that $Q = Q_c$ was found by a Newton–Raphson method, where $|Q - Q_c|/Q_c < 10^{-5}$ was used as the convergence criterion. Again, the agreement between the two sets of results was good over the entire range of Ca (relative error less than 1%).

3.2. Square tube

In a square tube, the finger radius also increases as the capillary number decreases, but cannot be greater than the minimum cross-sectional radius of the tube. Hence, below a certain value of the capillary number, \widehat{Ca} , the air–liquid interface far behind the bubble tip must become non-axisymmetric and draining flows develop that drive the fluid into distinct lobes.

3.2.1. Draining flows

The development of draining flows and corresponding changes in interface shape with increasing axial distance from the finger tip are shown in figure 6(a–d) for a capillary number of 0.007. The first cross-section is at $x_3 = 0.7$, less than one half-width downstream of the finger tip. In this region, the interface is approximately axisymmetric, but transverse flows can be seen to be driving fluid into the corner of the square and a dimensionless pressure gradient of about 35 has developed between the sides and corner of the cross-section. At the next cross-section, $x_3 = 1.2$, the interface has become non-axisymmetric and the transverse pressure gradient has increased enormously to a value of approximately 235. At $x_3 = 1.7$, the magnitude of the draining flows is reduced and a constant-pressure lobe is beginning to develop at the sides of the cross-section. Finally, by $x_3 = 2.2$, the pressure drop is confined to a small thin-film region that connects the two constant-pressure lobes, and there is very little fluid motion. The further details of the evolution are described (in the limit of

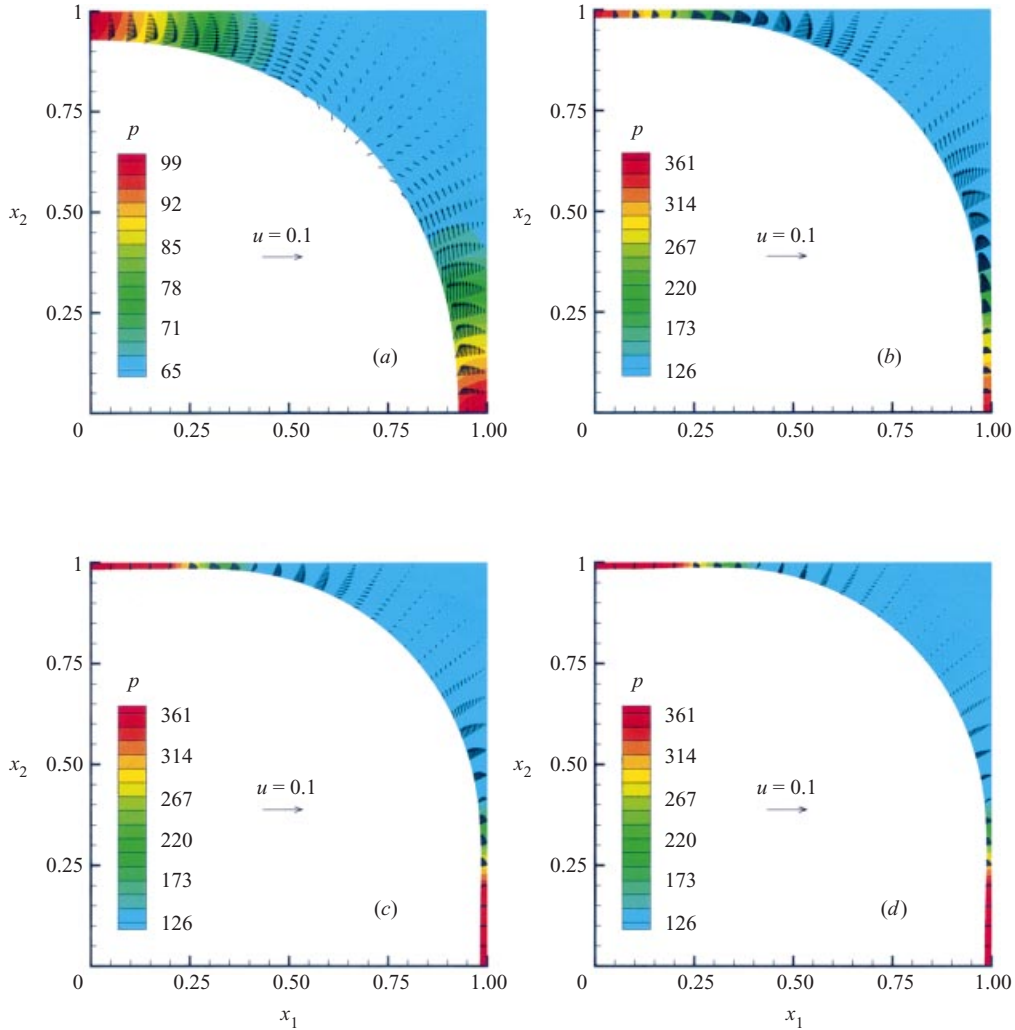


FIGURE 6. Draining flows developing in a tube of square cross-section at a capillary number of 0.007. Transverse cross-sections are shown at axial distances (a) 0.7, (b) 1.2, (c) 1.7 and (d) 2.2 from the bubble tip. The vectors indicate transverse velocities and the colour contours represent the pressure. The vector scale is always the same, but the pressure scale differs from cross-section to cross-section. The film becomes thinner as x_3 increases.

small capillary number) by Wong *et al.* (1995a) but are hard to resolve numerically because of the extreme thinning of the film and the very long axial length scales required for significant film rearrangement.

3.2.2. A tip asymmetry

Figure 7(a) shows the effect of capillary number upon the radius of the air finger at a distance 11 half-widths behind the finger tip; r_h is the radius measured in the horizontal plane $x_1 = 0$ and r_d is the radius measured in the diagonal plane $x_1 = x_2$. The divergence of the two radii at low Ca ($Ca < \widehat{Ca}$) demonstrates that the interface has become non-axisymmetric in this regime and the data are in good qualitative agreement with the experimental measurements of Kolb & Cerro (1991)

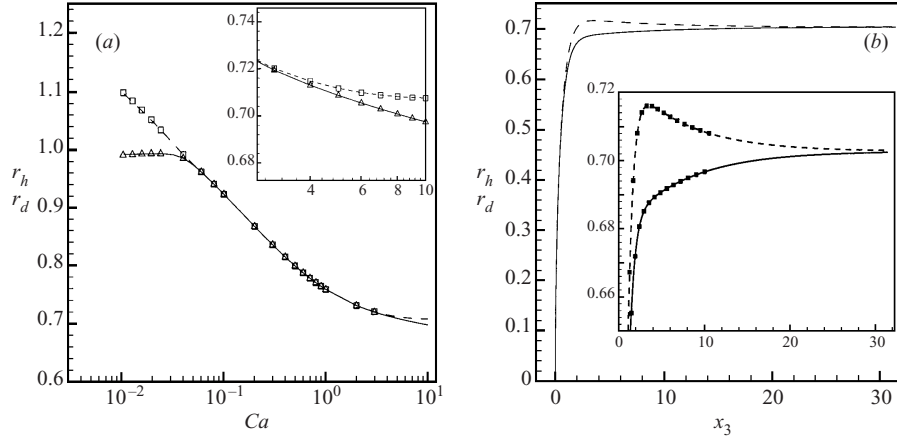


FIGURE 7. Results in a square tube: (a) Finger radii, r_h (solid) and r_d (dashed) vs. capillary number. The radii are measured 11 half-widths behind the finger tip. The symbols show the same results r_h (triangles) and r_d (squares), computed on a refined mesh. The inset graph is an enlargement of the results at high Ca . (b) Finger radii, r_h (solid) and r_d (dashed) plotted against axial distance x_3 for $Ca = 10$. The inset graph shows the same data, but with results for a shorter computational domain overlaid as boxes.

and the theoretical predictions of Ratulowski & Chang (1989), who found $\widehat{Ca} \approx 0.04$ (based on a numerical solution of the equations of lubrication theory in the arc-length formulation).

The unexpected divergence of the two radii for $Ca > 4$ in figure 7(a), see inset, is a consequence of a previously unobserved phenomenon: an asymmetry in the region of the bubble tip at high Ca . This asymmetry is illustrated in figure 7(b) which shows the shape of the air–liquid interface in the two planes $x_1 = 0$ and $x_1 = x_2$ for $Ca = 10$. The interface is noticeably non-axisymmetric immediately behind the finger tip, but eventually decays to an axisymmetric state.

The tip asymmetry is caused by the non-axisymmetric passage of fluid around the finger tip. In square tubes, the fluid particles tend to move towards the corners, which offer less resistance to the flow than the thinner regions along the sides of the tube. The ensuing transverse flows induce a transverse pressure gradient that lowers the fluid pressure in the corners, where the air–liquid interface moves radially outwards. In the region behind the bubble tip, surface tension acts to restore the air–liquid interface to an axisymmetric shape, and the non-uniform pressure distribution continues to drive fluid into the corner until $r_d = r_h$. Thus, the flow towards the corner that originally caused the non-axisymmetry to develop also restores the interface to an axisymmetric shape.

As Ca increases, surface tension becomes relatively weaker and the decay rate of the tip asymmetry decreases. In figure 7(a), the radii were measured 11 half-widths behind the finger tip. For $Ca > 4$ the interface is still visibly non-axisymmetric at this position. Repeating the calculations using a longer domain indicates that at a distance 32 half-widths behind the finger tip the interface remains axisymmetric until $Ca > 8$, when the tip asymmetry again becomes noticeable.

Incidentally, the inset graph in figure 7(b) demonstrates that the results in a short computational domain are indistinguishable from those in a longer one. Thus, despite the fact that the short domain is not long enough to resolve the decay to the

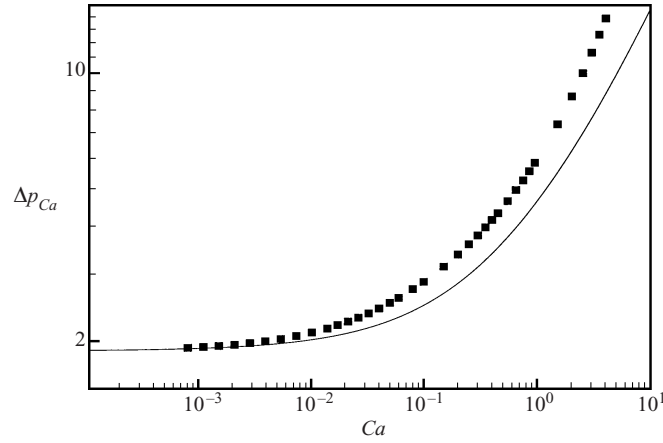


FIGURE 8. Pressure drop (boxes) across the bubble tip (on capillary scale) in a square tube vs. capillary number. The line is the asymptotic prediction of Wong *et al.* (1995b), valid as $Ca \rightarrow 0$.

axisymmetric state, the boundary conditions, described in §2.1, capture the correct behaviour without the need to match to decaying eigenfunctions explicitly.

The computations indicate that the decay rate of the tip asymmetry also decreases as $Ca \rightarrow \widehat{Ca} \approx 0.033$. This decrease is due to the extreme thinning of the film as $r_h \rightarrow 1$ and the corresponding very slow draining flows from the sides into the corner. Details of the calculation of \widehat{Ca} are shown in Appendix B.

3.2.3. Pressure drops

In practical applications, one of the most important parameters is the pressure drop across the bubble tip. Ratulowski & Chang's (1989) lubrication-theory-based study predicted that, at low Ca , the pressure drop over the tip of a long bubble moving through a square tube would be higher than in a circular tube of the same width.

In contrast, Wong *et al.* (1995b) argued that the reduced contact between the bubble and tube wall in a square tube, compared to a circular tube, should lead to reduced drag and hence a lower pressure drop across the bubble tip. They estimated pressure drops by perturbing about numerically calculated static equilibrium shapes and using the method of matched asymptotic expansions. The pressure drop across the bubble tip in a square tube was found to be

$$\Delta p_{Ca} = 1.8862 + 2.75 Ca^{2/3} \quad \text{as } Ca \rightarrow 0, \quad (3.2)$$

where the pressure drop is again non-dimensionalized on the capillary scale. This expression is compared to our numerical results in figure 8.

At $Ca = 0.00081$ (the limit of our computations) the relative error between the numerical solution and equation (3.2) is approximately 0.5%, but by $Ca = 0.01$ the difference has increased to 5%. In axisymmetric geometries, the discrepancies between small- Ca asymptotic predictions and numerical solutions are of similar magnitudes (Reinelt & Saffman 1985; Giavedoni & Saita 1997) and we may conclude that for this type of problem, lubrication theory is only accurate at very small capillary numbers. In the square capillary, the asymptotic predictions systematically underestimate the pressure drop across the bubble tip whereas the opposite is true for flows in circular tubes; see figure 4(b). Nonetheless, our results confirm the scaling of Wong *et al.* (1995b) and demonstrate that, at all values of Ca , the pressure drop over the bubble

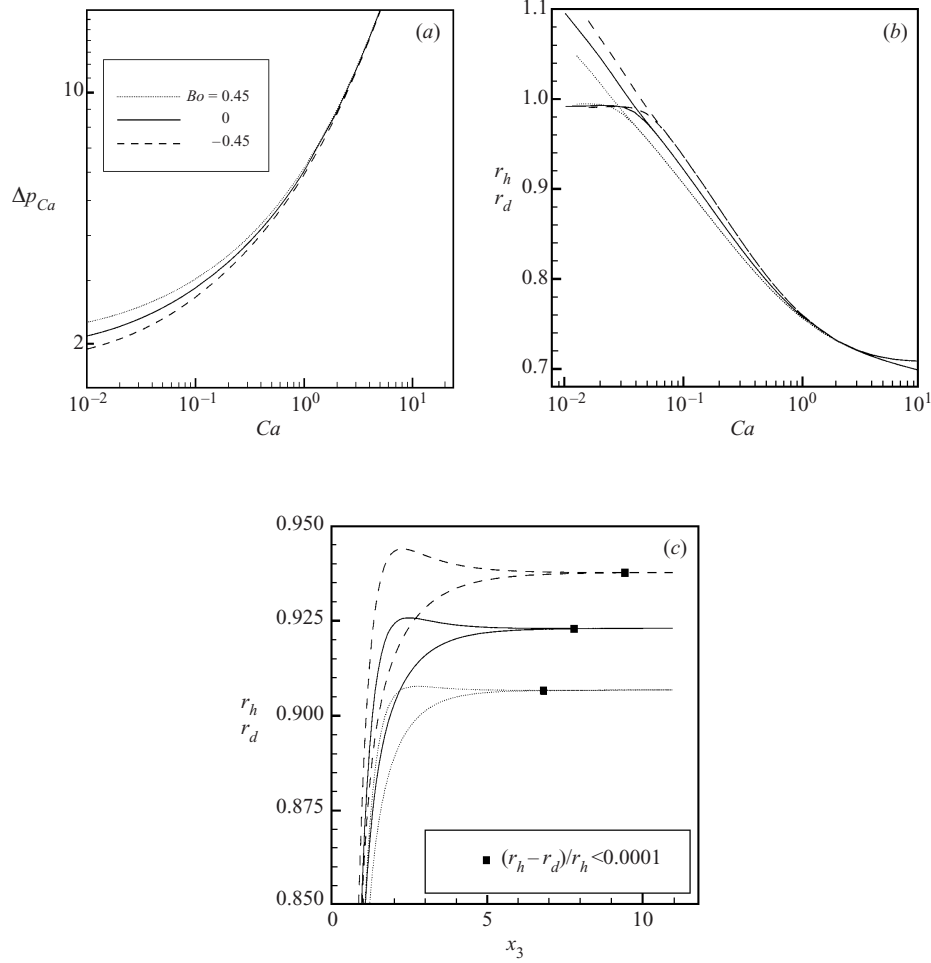


FIGURE 9. Effects of gravity in a square tube: (a) Pressure drop across the bubble tip on the capillary scale and (b) finger radii, r_h and r_d vs. capillary number. The radii are measured 11 half-widths behind the finger tip. The results for $Bo = 0.45$ and $Bo = -0.45$ are shown as well as $Bo = 0$. (c) Finger radii, r_h and r_d plotted against axial distance x_3 for $Ca = 0.1$. The results for $Bo = 0.45$ (dotted) and $Bo = -0.45$ (dashed) are shown as well as $Bo = 0$ (solid). For each case, the box marks the axial position at which the relative difference between the two radii $(r_h - r_d)/r_h$ is 0.01%.

tip is smaller in a square capillary than in a circular capillary of the same transverse length scale.

3.2.4. Gravitational effects

The inclusion of gravity causes changes in the film thickness and pressure drop at a given capillary number, much as in the axisymmetric problem. Figure 9(a, b) shows the pressure drop across the bubble tip and the two finger radii, r_h and r_d , measured 11 half-widths behind the finger tip against Ca for the values of the Bond number used in Kolb & Cerro's (1991) experiments: $Bo = 0$, -0.45 and 0.45 .

As in the axisymmetric case, at high values of Ca , the effects of gravity become negligible. At low Ca , gravity affects the film thickness and alters the value of \widehat{Ca} . At a given Ca , a positive Bond number causes the film to become thicker. Hence, \widehat{Ca} decreases with an increase in Bond number, see figure 9(b).

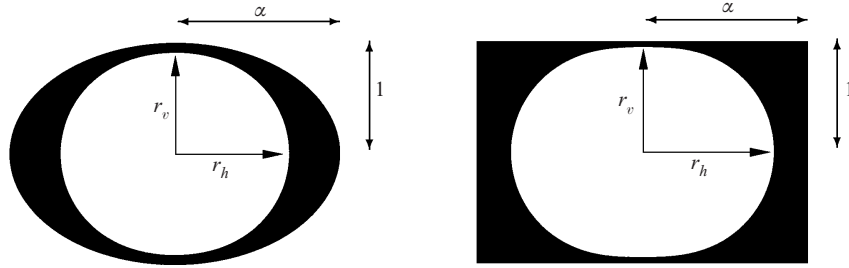


FIGURE 10. Computed interface cross-sections in elliptical and rectangular tubes for $Ca = 0.15$ and $\alpha = 1.5$. The cross-sections are taken at $x_3 = 10$. The reference length scale is the shortest semi-axis in each case.

The changes in film thickness also affect the decay rates of the tip asymmetry at given values of Ca , see figure 9(c). For positive Bo , the film is thicker and fluid will drain into the corner more quickly. Hence, the decay to the axisymmetric equilibrium state is achieved over a shorter axial length. The opposite is true for negative Bo , where the reduced film thickness decreases the decay rate. These effects are most clearly seen by comparing the axial locations of the three boxes in figure 9(c). For each case, the box marks the position at which the relative difference between the r_h and r_d is 0.01%. As the film thickness decreases, the decay rate decreases and the boxes move further from the finger tip.

3.3. Rectangular and elliptical tubes

In rectangular and elliptical tubes an extra control parameter enters the problem: the aspect ratio of the tube, α . In the following, the aspect ratio is always altered by changing the semi-axis in the horizontal plane, $x_1 = 0$ and keeping the other semi-axis equal to unity, see figure 10. The effects of gravity are similar to those in circular and square tubes and, in the interests of brevity, we present data only for $Bo = 0$.

3.3.1. Interface shapes

If the tube's aspect ratio differs from 1, the fluid film will be thicker along the longer of the two semi-axes of the tube. The thicker film offers less resistance to the fluid as it passes the finger tip and so fluid is driven from the shorter semi-axis towards the longer. This causes the interface to become non-axisymmetric close to the finger tip, as in the case of the square tube. The finger radius corresponding to the longer semi-axis, always r_h in our computations, becomes greater than that corresponding to the shorter, r_v . Again, surface tension acts to restore the air–liquid interface to an axisymmetric state and fluid continues to flow towards the longer semi-axis, causing r_h to decrease and r_v to increase with increasing axial distance. At high values of Ca , the interface eventually becomes axisymmetric far downstream, but at low Ca , r_v approaches 1 and an axisymmetric equilibrium state cannot exist.

Figure 11 shows the finger radii, r_h and r_v , plotted against Ca for rectangular and elliptical tubes. The general trends are the same in both cases. At a given value of Ca , an increase in aspect ratio causes an increase in finger radius and hence a decrease in film thickness in the plane of the shorter semi-axis. The value of \widehat{Ca} at which the equilibrium interface shape becomes non-axisymmetric increases with increasing aspect ratio, a direct result of this film thinning. The thinner films also lead to a decrease in the decay rate of the tip asymmetry which becomes more and more evident at high values of Ca and high values of α . In fact, figure 11(a) shows

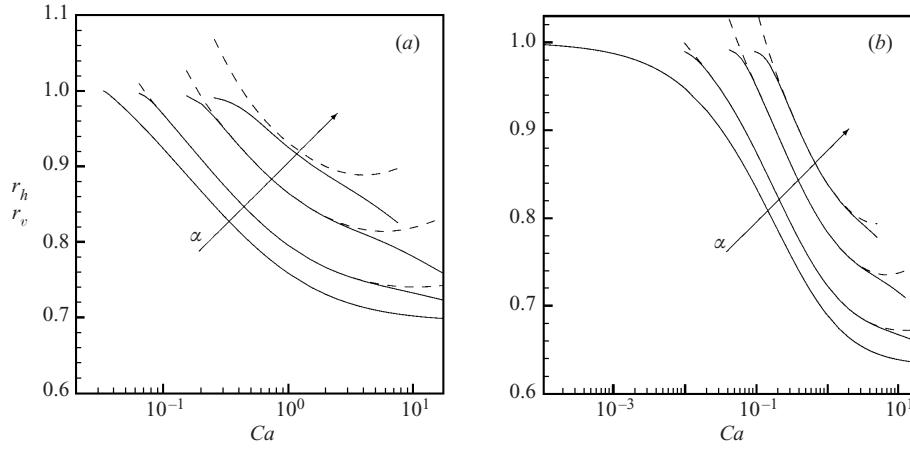


FIGURE 11. Finger radii, r_v (solid) and r_h (dashed) vs. capillary number for the aspect ratios 1, 1.1, 1.3 and 1.5: (a) rectangular tube, (b) elliptical tube. The radii are measured at a distance 100 times the shorter semi-axis behind the finger tip. The aspect ratio is altered by increasing the semi-axis corresponding to r_h and keeping the other fixed at unity. α increases in the direction of the arrows.

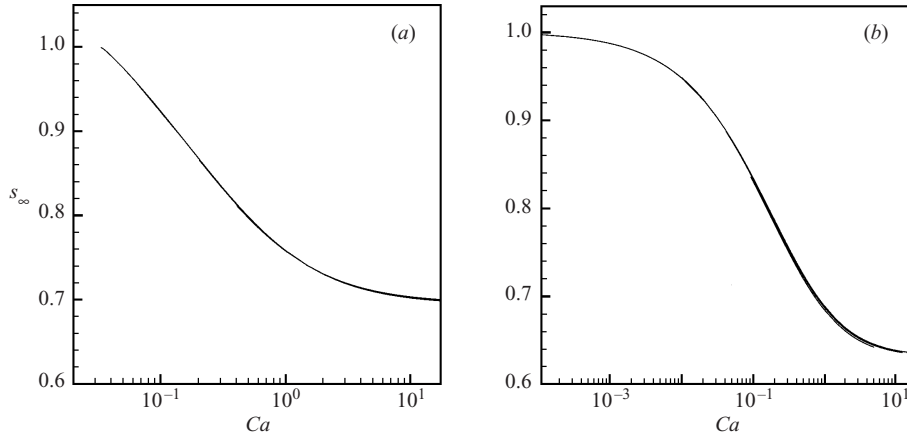


FIGURE 12. Scaled finger radius at infinity, s_∞ , vs. capillary number for the aspect ratios 1, 1.1, 1.3 and 1.5: (a) rectangular tube, (b) elliptical tube. The scaled finger radius is obtained by scaling the asymptotic finger radius, r_∞ , by the square-root of the aspect ratio. For the rectangular tube, the rescaling works so well that the scaled radii for different aspect ratios are almost indistinguishable.

that in a rectangular tube with $\alpha = 1.5$, the interface is noticeably non-axisymmetric, at all Ca , a distance 100 times the shorter semi-axis behind the finger tip.

3.3.2. A rescaling for the asymptotic finger radii in non-axisymmetric tubes

In regimes in which the interface is axisymmetric, figure 11 suggests a certain similarity between the general shapes of the curves at different aspect ratios. Motivated by this observation, we found that a linear rescaling of the form

$$s_\infty \equiv r_\infty \alpha^{-1/2} \quad (3.3)$$

collapses the data onto the line $\alpha = 1$, for both rectangular, figure 12(a), and elliptical tubes, figure 12(b). Here r_∞ is the axisymmetric bubble radius infinitely far behind the bubble tip. It is calculated from the flow rate in the computational domain, Q , by

using the relation $r_\infty = 2\sqrt{(\alpha - Q)/\pi}$ for the rectangle, and $r_\infty = \sqrt{(\pi\alpha - 4Q)/\pi}$ for the ellipse.

The agreement between the scaled radii is remarkable and it appears to be near perfect in the rectangular tubes. In fact, the scaled radii for different aspect ratios are almost indistinguishable. In elliptical tubes, the agreement is not as good and the error increases with aspect ratio. At $\alpha = 1.5$, however, the relative error is less than 1% over the range of Ca for which the interface is axisymmetric. It must be stressed that the scaling (3.3) is purely empirical and only applies to the finger radii far behind the bubble tip. In fact, the shape of the air–liquid interface near the bubble tip varies considerably with α . Therefore, the rescaling does not indicate similarity between the overall finger shapes for different values of α .

The rescaling (3.3) has a simple physical interpretation for rectangular tubes of differing aspect ratios but the same cross-sectional area: if air is injected at a constant volumetric flow rate, the propagation speed, and hence the radii, of the resulting air fingers will be the same in every tube, provided that the ultimate equilibrium state of the air–liquid interface is axisymmetric. This result is also true for elliptical tubes of moderate aspect ratio.

This rescaling allows us to conjecture that as the aspect ratio increases there will be an aspect ratio, $\hat{\alpha}$ beyond which no axisymmetric equilibrium solution exists and the scaling breaks down. This follows from the observation that for both the circular and square tubes the finger radii approach a (different) minimum value as Ca increases, $r_\infty^{(\min)} = \lim_{Ca \rightarrow \infty} r_\infty(\alpha = 1)$. If the rescaled minimum radius, $s_\infty^{(\min)}$, is greater than $\alpha^{-1/2}$, then an axisymmetric interface cannot fit inside the tube. The aspect ratio, $\hat{\alpha}$, may therefore be calculated by solving the equation

$$s_\infty^{(\min)} = r_\infty^{(\min)} = \frac{1}{\sqrt{\hat{\alpha}}}. \quad (3.4)$$

In the case of the square tube, $r_\infty^{(\min)} \approx 0.7$, from which it follows that $\hat{\alpha} \approx 2.04$ for rectangular tubes.

To check this prediction, we computed $\widehat{Ca}(\alpha)$ for elliptical and rectangular tubes, see figure 16 in Appendix B. \widehat{Ca} was found to increase with increasing α and ultimately appears to approach an asymptote as $\alpha \rightarrow \hat{\alpha}$. In elliptical tubes, \widehat{Ca} approaches an asymptote as $\alpha \rightarrow 2.65$, whereas equation (3.4) predicts $\hat{\alpha} = 2.48$. This shows again that the scaling (3.3) is poorer for elliptical tubes.

3.3.3. Pressure drop

Wong *et al.* (1995a,b) considered the propagation of bubbles in rectangular tubes and found that the pressure drop across the bubble tip has the form $\Delta p_{Ca} = A + B Ca^{2/3}$ as $Ca \rightarrow 0$, where A and B are constants that depend upon the aspect ratio. Figure 13 compares our numerical results with the asymptotic predictions for rectangular tubes of aspect ratio $\alpha = 1.2$ and 2. The results are again in good agreement only at very small values of Ca (relative error $\approx 0.5\%$ at $Ca = 0.00081$). At higher values of Ca , the asymptotic predictions underestimate the pressure drops, just as in the square tube.

Increasing the aspect ratio leads to a decrease in pressure drop across the bubble tip in both ellipses and rectangles, see figure 14. Furthermore, the pressure drop across the bubble tip in a rectangular tube is always lower than that in an elliptical tube of the same aspect ratio and transverse length scale, presumably because of the reduced contact between the bubble and the walls in the former case.

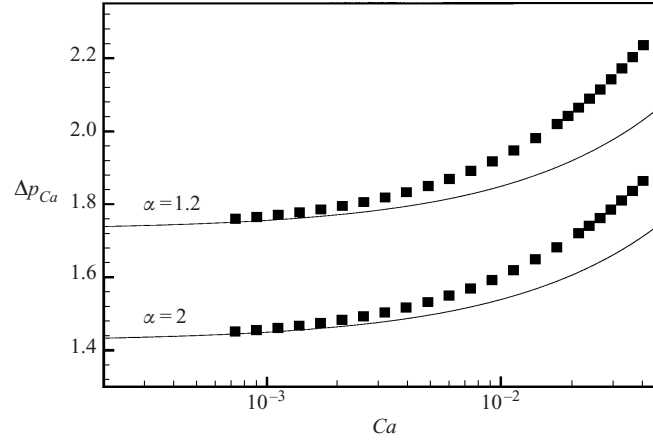


FIGURE 13. Pressure drop across the finger tip for rectangular tubes of different aspect ratio. Our numerical results (boxes) are plotted together with the low- Ca asymptotic result of Wong *et al.* (1995b) (solid lines).

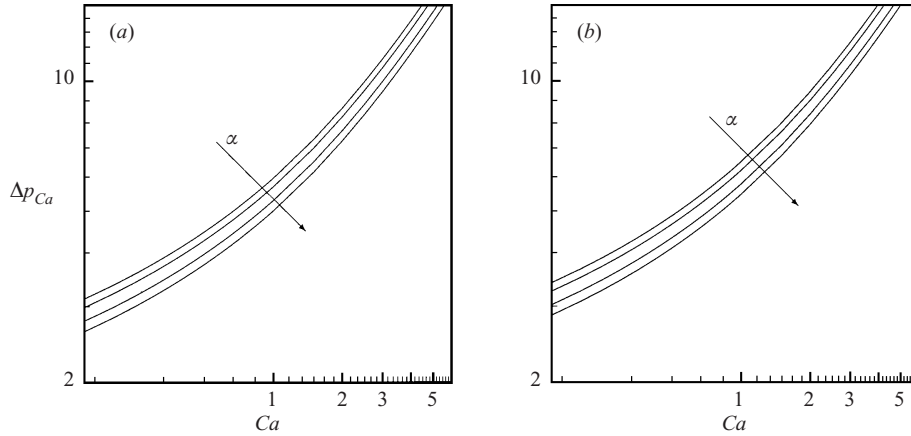


FIGURE 14. Pressure drop across the bubble tip (on capillary scale) vs. capillary number for the aspect ratios 1, 1.1, 1.3 and 1.5: (a) rectangular tube, (b) elliptical tube. The aspect ratio is altered by increasing the semi-axis corresponding to r_h and keeping the other fixed at unity. α increases in the direction of the arrows.

The rescaling for the asymptotic finger radii, see §3.3.2, may be interpreted as a rescaling for the pressure jump across the interface far behind the bubble tip. The pressure drops across the bubble tip also appear to be similar, see figure 14. We find that to high accuracy the pressure drop in an elliptical or rectangular tube of aspect ratio α may be calculated from the $\alpha = 1$ curve by a linear rescaling of the form

$$\Delta p_{Ca}(\alpha, Ca) = f(\alpha) \Delta p_{Ca}(\alpha = 1, Ca). \quad (3.5)$$

In this case, we can find no simple functional form for $f(\alpha)$, but table 1 lists values of $f(\alpha)$ for a number of values of α . The values are the same for rectangles and ellipses, within the accuracy of two decimal figures. In the rectangular case the results collapse onto those of the square and in the elliptical case they collapse onto those of the circle.

Again, the scaling is empirical, but its accuracy is comparable to the scaling for

| | | | | | | | |
|-------------------------------------|---|-------|-------|-------|-------|-------|-------|
| α | 1 | 1.1 | 1.2 | 1.3 | 1.5 | 1.7 | 2 |
| $f(\alpha)$ | 1 | 0.96 | 0.92 | 0.89 | 0.84 | 0.80 | 0.76 |
| $g(\alpha) = \alpha^{1/2}f(\alpha)$ | 1 | 1.007 | 1.008 | 1.015 | 1.029 | 1.043 | 1.075 |

TABLE 1. Values of the function $f(\alpha)$: the ratio of pressure drop across the bubble tip in a tube of aspect ratio α to the $\alpha = 1$ result; and $g(\alpha) = \alpha^{1/2}f(\alpha)$: the result rescaled to apply to tubes of constant cross-sectional area.

| α | Ellipse | | Rectangle | |
|----------|---------|--------|-----------|--------|
| | Q_T | Ca_T | Q_T | Ca_T |
| 1 | 0.393 | 0.691 | 0.523 | 0.680 |
| 1.1 | 0.432 | 0.688 | 0.575 | 0.675 |
| 1.3 | 0.511 | 0.666 | 0.675 | 0.642 |
| 1.5 | 0.589 | 0.631 | 0.772 | 0.592 |

TABLE 2. Values of the flow rate and capillary number at which the flow undergoes a kinematic transition from complete bypass to recirculation.

the asymptotic finger radii. The relative error between results scaled using the data in table 1 and the exact computations is within 1% over the entire range of Ca . Considering the limit $Ca \rightarrow 0$, it follows that $f(\alpha)$ must be approximately equal to the ratio of mean curvatures of the corresponding static equilibrium meniscus shapes. Wong *et al.* (1995a) have calculated such curvatures numerically for a number of tube geometries and the appropriate ratios for rectangular tubes do indeed agree with the values of $f(\alpha)$ presented above.

It is important to recall that a change in α changes the cross-sectional area of the tube. The results for tubes of constant cross-sectional area, but different aspect ratios, are obtained on multiplication of Δp_{ca} by $\alpha^{1/2}$. If $\alpha > 1$, $g(\alpha) \equiv \alpha^{1/2}f(\alpha) > 1$, see table 1, and $g(\alpha)$ increases monotonically with α . It follows that in tubes of equal cross-sectional area, the pressure drop increases with aspect ratio, albeit only slightly.

3.4. Flow fields

In all geometries, the volume flux past the bubble decreases with decreasing capillary number. Taylor (1961) showed by purely kinematic arguments that at sufficiently small flow rates, a recirculating flow region (in the moving frame of reference) must exist ahead of the bubble tip. The fluid near the wall is always directed towards the bubble, but at low flow rates the fluid near the centreline will be directed away from the tip, creating a recirculating flow region. The flow rate at which the axial velocity on the tube's centreline far ahead of the bubble tip changes sign, Q_T , can be determined from the exact solutions for Poiseuille flow in elliptical and rectangular tubes (e.g. White 1991, pp. 119–120). Table 2 presents the values of Q_T and the capillary numbers at which this transition occurs, Ca_T , for bubbles propagating in elliptical and rectangular tubes of different aspect ratios in the absence of gravity. If $Bo \neq 0$, Q_T remains unchanged, but Ca_T decreases with increasing Bo .

For flows in axisymmetric tubes, the line S on the bubble surface which separates the recirculating flow region from the region in which fluid passes around the bubble is a stagnation line. In non-axisymmetric tubes there are significant transverse flows on the bubble surface and the fluid only comes to rest at a small number of stagnation points. This is illustrated in figure 15 for the flow past a bubble in a rectangular tube

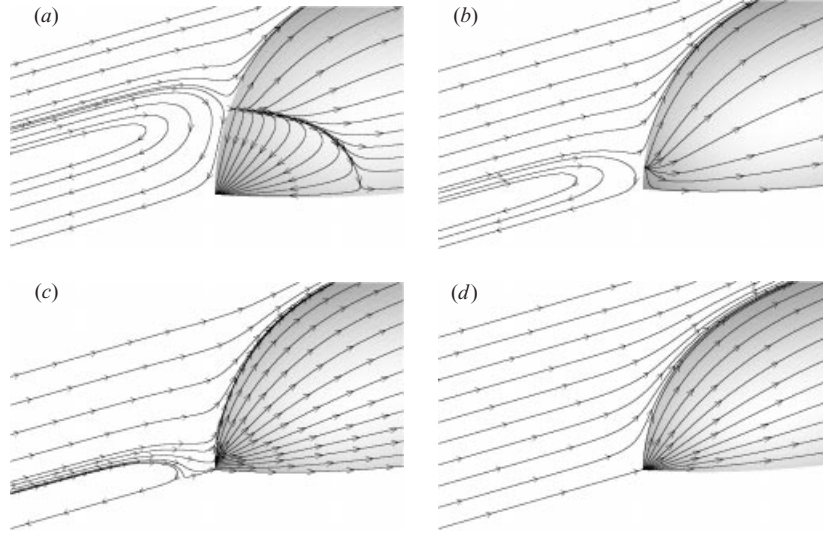


FIGURE 15. Streamlines in the moving frame of reference for a rectangular tube $\alpha = 1.5$ (a) $Ca = 0.2$, (b) $Ca = 0.5$, (c) $Ca = 0.55$, (d) $Ca = 2.0$. Streamlines are shown on the surface of the bubble and in the plane along the shorter semi-axis, $x_2 = 0$.

of aspect ratio $\alpha = 1.5$. Four generic flow regimes can be identified. At low capillary numbers, figure 15(a), there are five stagnation points (nine for a square tube), one at the bubble tip and four (eight) at a finite radial distance in the planes of symmetry. In the classification of Lighthill (1963) and Tobak & Peake (1982), the stagnation point on the centreline is a ‘point of separation’; the line S which connects the outer stagnation points is a ‘line of attachment’. In non-axisymmetric geometries the line S is not a stagnation line but it cannot be crossed by any fluid particles on the bubble surface. As Ca increases, the stagnation points move towards the centreline and a topological change occurs when the stagnation points on the symmetry plane dividing the shorter semi-axes coincide with the stagnation point at the tip, figure 15(b). This regime does not occur when $\alpha = 1$ because there must be symmetry about the line $x_1 = x_2$. As Ca increases yet further, the stagnation points on the other symmetry plane eventually coincide at the tip and then move onto the centreline ahead of the bubble, figure 15(c). This structure was first conjectured by Taylor (1961), but it was not observed until the recent axisymmetric computations of Giavedoni & Saita (1997). Finally, for $Ca > Ca_T$, there is only one stagnation point at the bubble tip and there is no fluid recirculation.

4. Summary and further discussion

We have investigated the propagation of long bubbles into tubes of elliptical and rectangular cross-section, including the special cases of circular and square tubes. For flows in rectangular tubes, we were able to confirm Wong *et al.*'s (1995b) asymptotic predictions for the pressure drop across the bubble tip in the limit $Ca \rightarrow 0$, $Bo = 0$. At higher values of the capillary number, the asymptotic theory underestimates the pressure drop, a contrast to the theory in circular tubes, which overpredicts this quantity.

In all geometries, the main effect of gravity is to alter the thickness of the fluid film deposited behind the finger tip. If the bubble is travelling upwards, additional fluid

accumulates in the film and both the pressure drop across the finger tip and the flow past the bubble increase at a given Ca . If the bubble is being driven downwards, the film becomes thinner with concomitant decreases in the flow past the bubble and pressure drop. In every case, gravitational effects become negligible as Ca increases.

At given Ca and Bo , the pressure drop over the bubble tip in a rectangular tube is always lower than that in an elliptical tube of the same aspect ratio and transverse length scale. For tubes of the same transverse length scale, the pressure drop decreases with increasing aspect ratio. For tubes of the same cross-sectional area, however, the pressure drop increases (slightly) with increasing aspect ratio. This result could have important implications in the airway reopening problem.

Wong *et al.*'s (1992) calculations of static bubbles shapes have already shown that the air–liquid interface in rectangular tubes is non-axisymmetric at $Ca = 0$. In non-circular tubes, we find that the air–liquid interface develops a noticeable asymmetry near the tip of the air finger at all values of the capillary and Bond numbers. The tip asymmetry at finite Ca is caused by the non-axisymmetric passage of fluid around the tip and is, therefore, not the same as the static asymmetry. In tubes of moderate aspect ratio, at high values of the capillary number, the interface eventually approaches an axisymmetric equilibrium configuration, although the decay rates can be very slow.

Below a particular value of the capillary number, $\widehat{Ca}(\alpha, Bo)$, there is no axisymmetric equilibrium state and the interface remains non-axisymmetric. In both elliptical and rectangular tubes, there is a value of the aspect ratio, $\hat{\alpha}$, above which the equilibrium interface shape is always non-axisymmetric. The value of \widehat{Ca} might be of interest in industrial coating processes because if $Ca < \widehat{Ca}$ dry regions may develop on the tube wall after passage of the finger. In practice, the development of dry spots will depend crucially upon an interplay among the curing time of the fluid, the time taken for the fluid to drain into lobes and the Van der Waals forces that cause film rupture. The theoretical values of \widehat{Ca} determined in Appendix B were calculated assuming an infinitely thin film at an infinite distance behind the finger tip. The action of Van der Waals forces will cause film rupture a finite distance behind the tip at values of $Ca > \widehat{Ca}$.

In non-axisymmetric tubes we find four different flow regimes, three of which contain a region of reversed flow in the frame moving with the bubble tip. The capillary number above which the reversed flow disappears, Ca_T , decreases with increasing aspect ratio and increasing Bond number. Ca_T is always lower in rectangular tubes, than in elliptical tubes of the same aspect ratio. Thus, the circular tube contains a region of recirculating flow for the largest range of Ca . The changes in the flow topology could be of importance in problems in which the air–liquid interface is contaminated by a significant amount of surfactant. In this situation, the surface tension depends on the surfactant concentration, determined by an advection–diffusion process on the air–liquid interface. If the advective process dominates, the different surface flow fields may lead to noticeable variations in the surface tension along the interface.

Perhaps the most surprising result is the discovery of a rescaling, based upon the aspect ratio, that collapses the finger radius far behind the bubble tip in rectangular tubes at a given Ca onto that in the square tube at the same Ca . The rescaling is only applicable to axisymmetric equilibrium shapes, i.e. for $Ca < \widehat{Ca}$, but appears to be near perfect. In the case of elliptical tubes, the same rescaling collapses the interface radius onto that in the circular tube, but as α increases the scaling loses accuracy. The physical interpretation of the rescaling is that for rectangular tubes of the same

cross-sectional area, the propagation speed of the air finger, driven by injection of air at a constant volumetric rate, is independent of the aspect ratio. The result only holds if the equilibrium shape of the air–liquid interface is axisymmetric, however, and so once $\alpha > \hat{\alpha}$ it no longer applies.

Furthermore, the pressure drop across the bubble tip in a rectangular/elliptical tube of aspect ratio α may be estimated from the pressure drop in a square/circular tube. For all the aspect ratios we have examined ($\alpha \leq 2$) the ratio between the mean curvatures of the static interface shapes is always approximately equal to the ratio of the pressure drops across the tip at any Ca (relative error within 1%). The functional form of the pressure drop– Ca relationship, therefore, appears to be independent of the precise details of the tube geometry, as previously demonstrated by Wong *et al.* (1995b) at small Ca .

Financial support from the EPSRC is gratefully acknowledged. The authors would also like to thank D. A. Reinelt for supplying his numerical results and the anonymous referees for their valuable comments which have helped to improve earlier versions of the manuscript. The HSL library routine MA42: a frontal solver for sparse, unsymmetric systems and the cfortran.h header file were used in the development of the numerical code in this work.

Appendix A. Convergence of numerical results

Table 3 shows a convergence study in a square tube. The pressure drop across the bubble tip, Δp_{Ca} , finger radii, r_h and r_d , measured 11 half-widths behind the finger tip, and flow rate through the computational domain, Q , are shown at a number of different values of the capillary number, Ca . The coarse and fine meshes consist of 19 706 and 39 680 degrees of freedom, respectively. The relative error between the two sets of results is within 0.5% for all parameters. Note the development of the tip asymmetry at $Ca = 3$.

Appendix B. Calculation of \widehat{Ca}

The rescaling (3.3) only applies in situations in which the air finger becomes axisymmetric far behind the bubble tip, i.e. for $Ca < \widehat{Ca}$. Thus, \widehat{Ca} is defined to be the value of Ca for which an axisymmetric air–liquid interface touches the tube walls at an infinite distance behind the finger tip; so that, as $x_3 \rightarrow \infty$, the cross-sectional area of the fluid in one quarter of the tube will approach

$$\hat{A} = \begin{cases} \frac{1}{4}\pi(\alpha - 1) & \text{for elliptical tubes,} \\ \alpha - \frac{1}{4}\pi & \text{for rectangular tubes.} \end{cases} \quad (\text{B } 1)$$

In the absence of gravity, $u_3 \rightarrow 1$ as $x_3 \rightarrow \infty$ and so the flow rate in the computational domain at $Ca = \widehat{Ca}$ must equal \hat{A} . The flow rate is independent of the axial position and hence \widehat{Ca} may be calculated using relatively short computational domains. We used a Newton–Raphson method to determine the value of Ca for which $Q = \hat{A}$ and figure 16 shows the results for elliptical and rectangular tubes. \widehat{Ca} increases with α and ultimately approaches a vertical asymptote as $\alpha \rightarrow 2.04$ and $\alpha \rightarrow 2.65$ for rectangular and elliptical tubes, respectively.

| Ca | Coarse mesh | | | | Fine mesh | | | |
|------|-----------------|-------|-------|-------|-----------------|-------|-------|-------|
| | Δp_{Ca} | r_h | r_d | Q | Δp_{Ca} | r_h | r_d | Q |
| 0.01 | 2.10 | 0.992 | 1.10 | 0.130 | 2.10 | 0.990 | 1.10 | 0.130 |
| 0.02 | 2.23 | 0.993 | 1.05 | 0.173 | 2.23 | 0.993 | 1.05 | 0.173 |
| 0.03 | 2.34 | 0.992 | 1.01 | 0.206 | 2.34 | 0.991 | 1.01 | 0.206 |
| 0.04 | 2.43 | 0.985 | 0.991 | 0.232 | 2.43 | 0.985 | 0.991 | 0.232 |
| 0.05 | 2.52 | 0.973 | 0.975 | 0.255 | 2.52 | 0.973 | 0.975 | 0.255 |
| 0.06 | 2.59 | 0.961 | 0.961 | 0.274 | 2.59 | 0.961 | 0.961 | 0.274 |
| 0.07 | 2.67 | 0.950 | 0.950 | 0.291 | 2.66 | 0.950 | 0.950 | 0.291 |
| 0.08 | 2.73 | 0.940 | 0.940 | 0.306 | 2.73 | 0.940 | 0.940 | 0.306 |
| 0.09 | 2.80 | 0.931 | 0.931 | 0.319 | 2.79 | 0.931 | 0.931 | 0.319 |
| 0.1 | 2.86 | 0.923 | 0.923 | 0.331 | 2.85 | 0.923 | 0.923 | 0.331 |
| 0.2 | 3.36 | 0.867 | 0.867 | 0.409 | 3.36 | 0.867 | 0.867 | 0.409 |
| 0.3 | 3.77 | 0.835 | 0.835 | 0.452 | 3.77 | 0.835 | 0.835 | 0.452 |
| 0.4 | 4.14 | 0.814 | 0.814 | 0.479 | 4.13 | 0.814 | 0.814 | 0.479 |
| 0.5 | 4.47 | 0.799 | 0.799 | 0.499 | 4.47 | 0.799 | 0.799 | 0.499 |
| 0.6 | 4.79 | 0.787 | 0.787 | 0.514 | 4.78 | 0.787 | 0.787 | 0.514 |
| 0.7 | 5.10 | 0.778 | 0.778 | 0.525 | 5.09 | 0.778 | 0.778 | 0.525 |
| 0.8 | 5.40 | 0.770 | 0.770 | 0.534 | 5.39 | 0.770 | 0.770 | 0.534 |
| 0.9 | 5.69 | 0.764 | 0.764 | 0.542 | 5.68 | 0.764 | 0.764 | 0.542 |
| 1 | 5.97 | 0.758 | 0.758 | 0.548 | 5.96 | 0.758 | 0.758 | 0.548 |
| 2 | 8.67 | 0.731 | 0.731 | 0.581 | 8.65 | 0.731 | 0.731 | 0.581 |
| 3 | 11.3 | 0.719 | 0.720 | 0.593 | 11.2 | 0.719 | 0.720 | 0.593 |
| 4 | 13.8 | 0.713 | 0.715 | 0.600 | 13.8 | 0.713 | 0.715 | 0.600 |
| 5 | 16.4 | 0.709 | 0.712 | 0.604 | 16.4 | 0.709 | 0.712 | 0.604 |
| 6 | 18.9 | 0.705 | 0.710 | 0.607 | 18.9 | 0.705 | 0.710 | 0.607 |
| 7 | 21.5 | 0.703 | 0.709 | 0.609 | 21.4 | 0.703 | 0.709 | 0.609 |
| 8 | 24.0 | 0.701 | 0.708 | 0.610 | 24.0 | 0.701 | 0.708 | 0.610 |
| 9 | 26.6 | 0.699 | 0.708 | 0.611 | 26.5 | 0.699 | 0.708 | 0.611 |
| 10 | 29.1 | 0.697 | 0.708 | 0.612 | 29.0 | 0.697 | 0.708 | 0.612 |

TABLE 3. Convergence study in a square tube.

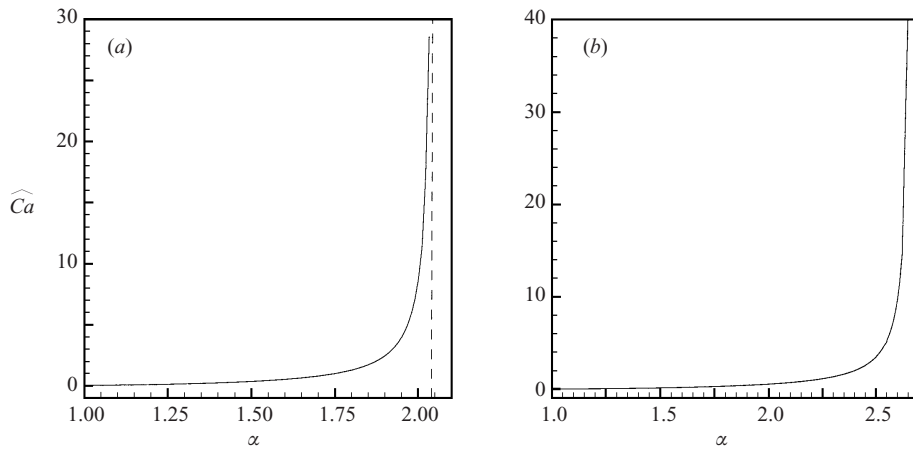


FIGURE 16. The capillary number \widehat{Ca} at which an axisymmetric air–liquid interface touches the tube walls as $x_3 \rightarrow \infty$ plotted as a function of aspect ratio α for (a) rectangular, and (b) elliptical tubes. In the case of the rectangular tube, the value of $\hat{\alpha}$ calculated from equation (3.4) is indicated as the dashed line.

REFERENCES

- BRETHERTON, F. P. 1961 The motion of long bubbles in tubes. *J. Fluid Mech.* **10**, 166–188.
- CHEN, J.-D. 1986 Measuring the film thickness surrounding a bubble inside a capillary. *J. Colloid Interface Sci.* **109**, 314–349.
- COX, B. G. 1962 On driving a viscous fluid out of a tube. *J. Fluid Mech.* **14**, 81–96.
- DUFF, I. S. & SCOTT, J. A. 1996 The design of a new frontal code for solving sparse, unsymmetric linear systems. *ACM Trans. Math. Software* **22**, 30–45.
- GAVER, D. P. I., HALPERN, D., JENSEN, O. E. & GROTEBERG, J. B. 1996 The steady motion of a semi-infinite bubble through a flexible walled channel. *J. Fluid Mech.* **319**, 25–56.
- GAVER, D. P. I., SAMSEL, R. W. & SOLWAY, J. 1990 Effects of surface tension and viscosity on airway reopening. *J. Appl. Physiol.* **369**, 74–85.
- GIAVEDONI, M. D. & SAITA, F. A. 1997 The axisymmetric and plane cases of a gas phase steadily displacing a Newtonian liquid – a simultaneous solution of the governing equations. *Phys. Fluids* **9**, 2420–2428.
- GOLDSMITH, H. L. & MASON, S. G. 1963 The flow of suspensions through tubes – ii. single large bubbles. *J. Colloid Interface Sci.* **18**, 237–261.
- HALPERN, D. & GAVER, D. P. I. 1994 Boundary element analysis of the time-dependent motion of a semi-infinite bubble in a channel. *J. Comput. Phys.* **115**, 366–375.
- HEIL, M. 2000 Finite Reynolds number effects in the propagation of an air finger into a liquid-filled flexible-walled tube. *J. Fluid Mech.* **424**, 21–44.
- HEIL, M. 2001 Finite Reynolds number effects in the Bretherton problem. *Phys. Fluids* **13**, 2517–2521.
- KISTLER, S. F. & SCRIVEN, L. E. 1983 Coating flows. In *Computational Analysis of Polymer Processing* (ed. J. R. A. Pearson & S. M. Richardson), pp. 243–299. London: Applied Science Publishers.
- KOLB, W. B. & CERRO, R. L. 1991 Coating the inside of a capillary of square cross section. *Chem. Engng Sci.* **46**, 2181–2195.
- KOLB, W. B. & CERRO, R. L. 1993 The motion of long bubbles in tubes of square cross section. *Phys. Fluids A* **5**, 1549–1557.
- LIGHTHILL, M. J. 1963 Attachment and separation in three-dimensional flows. In *Laminar Boundary Layers* (ed. L. Rosenhead), chap. II, § 2.6–2.7, pp. 72–82. Oxford University Press.
- PARK, C.-W. & HOMSY, G. M. 1984 Two-phase displacement in Hele Shaw cells: theory. *J. Fluid Mech.* **139**, 291–308.
- RATULOWSKI, J. & CHANG, H.-C. 1989 Transport of gas bubbles in capillaries. *Phys. Fluids A* **1**, 1642–1655.
- REINELT, D. A. 1987 The rate at which a long bubble rises in a vertical tube. *J. Fluid Mech.* **175**, 557–565.
- REINELT, D. A. & SAFFMAN, P. G. 1985 The penetration of a finger into a viscous fluid in a channel and tube. *SIAM J. Sci. Stat. Comput.* **6**, 542–561.
- RUSCHAK, K. J. 1980 A method for incorporating free boundaries with surface tension in finite element fluid-flow simulators. *Intl J. Num. Meth. Engng* **15**, 639–648.
- SCHWARTZ, L. W., PRINCEN, H. M. & KISS, A. D. 1986 On the motion of bubbles in capillary tubes. *J. Fluid Mech.* **172**, 259–275.
- SHEN, E. I. & UDELL, K. S. 1985 A finite element study of low Reynolds number two-phase flow in cylindrical tubes. *Trans. ASME: J. Appl. Mech.* **52**, 253–256.
- SINGHAL, A. K. & SOMMERTON, W. H. 1970 Two-phase flow through a non-circular capillary at low Reynolds numbers. *J. Can. Petrol. Technol.* **9**, 197–205.
- TAYLOR, C. & HOOD, P. 1973 A numerical solution of the Navier–Stokes equations using the finite element technique. *Computers Fluids* **1**, 73–100.
- TAYLOR, G. I. 1961 Deposition of a viscous fluid on the wall of a tube. *J. Fluid Mech.* **10**, 161–165.
- THULASIDAS, T. C., ABRAHAM, M. A. & CERRO, R. L. 1995 Bubble-train flow in capillaries of circular and square cross section. *Chem. Engng Sci.* **50**, 183–199.
- TOBAK, M. & PEAKE, D. J. 1982 Topology of three-dimensional separated flows. *Annu. Rev. Fluid Mech.* **14**, 61–85.
- WESTBORG, H. & HASSAGER, O. 1989 Creeping motion of long bubbles and drops in capillary tubes. *J. Colloid Interface Sci.* **133**, 135–147.
- WHITE, E. T. & BEARDMORE, R. H. 1962 The velocity of rise of single cylindrical air bubbles through liquids contained in vertical tubes. *Chem. Engng Sci.* **17**, 351–361.

- WHITE, F. M. 1991 *Viscous Fluid Flow*, 2nd edn. McGraw-Hill.
- WONG, H., MORRIS, S. & RADKE, C. J. 1992 Three-dimensional menisci in polygonal capillaries. *J. Colloid Interface Sci.* **148**, 317–336.
- WONG, H., RADKE, C. J. & MORRIS, S. 1995a The motion of long bubbles in polygonal capillaries. Part 1. Thin films. *J. Fluid Mech.* **292**, 71–94.
- WONG, H., RADKE, C. J. & MORRIS, S. 1995b The motion of long bubbles in polygonal capillaries. Part 2. Drag, fluid pressure and fluid flow. *J. Fluid Mech.* **292**, 95–110.